International Journal of Thermophysics manuscript No.
(will be inserted by the editor)

A Helmholtz Energy Equation of State for *trans*-1,1,1,4,4,4-Hexafluoro-2-butene [R-1336mzz(E)] and an Auxiliary Extended Corresponding States Model for the Transport Properties

Ryo Akasaka · Marcia L. Huber · Luke D. Simoni · Eric W. Lemmon

Received: date / Accepted: date

Ryo Akasaka

Department of Mechanical Engineering, Faculty of Science and Engineering, Kyushu Sangyo University, Fukuoka 8138503, Japan

Research Center for Next Generation Refrigerant Properties (NEXT-RP), International Institute for Carbon-Neutral Energy Research (WPI-I2CNER), Kyushu University, Fukuoka 8190395, Japan

E-mail: ryo-a@ip.kyusan-u.ac.jp

ORCID: 0000-0003-2641-6031

Marcia L. Huber

Applied Chemicals and Materials Division, National Institute of Standards and Technology, Boulder, CO 80305, USA

E-mail: marcia.huber@nist.gov

ORCID: 0000-0002-7976-741X

Luke D. Simoni

Thermal and Specialized Solutions, The Chemours Company, Newark, DE 19713, USA

E-mail: Luke.D.Simoni@chemours.com

Abstract This work presents a fundamental equation of state for the thermodynamic properties of R-1336mzz(E). The equation of state is expressed explicitly in the Helmholtz energy with temperature and density as the independent variables, and is based on consistent experimental datasets, including the critical parameters, vapor pressure, saturated liquid and vapor densities, (p, ρ, T) behavior, vapor-phase sound speed, and ideal-gas isobaric heat capacity. The equation of state is valid for temperatures from 200.15 K to 410 K and pressures up to 5.7 MPa. In this range, expected relative uncertainties at the 95 % confidence interval ($k = 2$) are 0.1 % for vapor pressures, 1 % for saturated liquid densities, 1 % for saturated vapor densities, 0.15 % for liquid densities, 0.5 % for vapor densities, and 0.05 % for vapor-phase sound speeds, except in the critical region where larger uncertainties of up to 2 % are sometimes observed in densities. The equation exhibits reasonable behavior in the critical and extrapolated regions; this is demonstrated by several plots of derived properties over wide ranges of temperature and pressure. Through the use of the new equation of state, this work also formulates an extended corresponding states (ECS) model for the viscosity and thermal conductivity of R-1336mzz(E) to represent recent experimental data for these properties mostly within their uncertainties.

Eric W. Lemmon

Applied Chemicals and Materials Division, National Institute of Standards and Technology, Boulder, CO 80305, USA

E-mail: eric.lemmon@nist.gov

ORCID: 0000-0002-0974-0203

Keywords Density · Equation of state · R-1336mzz(E) · Sound speed · Thermal conductivity · Vapor pressure · Viscosity

1 Introduction

The substance *trans*-1,1,1,4,4,4-hexafluoro-2-butene (CAS No. 66711-86-2), also known as R-1336mzz(E), is considered to be one of the next-generation refrigerants due to its zero-ozone depletion potential, ultra-low GWP, non-flammability characteristics, and favorable thermophysical properties. The molecular structure of R-1336mzz(E) is shown in Fig. 1, and the fundamental properties are summarized in Table 1. R-1336mzz(E) has the lowest normal boiling-point temperature (281.02 K) among hydrofluoroolefins (HFOs) in safety group of "A1" (no flame propagation and lower toxicity) according to the ANSI/ASHRAE safety classification [1]. Its non-flammable characteristic offers the possibility of large-scale waste-heat recovery applications such as high-temperature heat pumps and organic Rankine cycles [2–4]. The refrigerant blend R-471A, a ternary mixture of 78.7 mass fraction (%) *trans*-1,3,3,3-tetrafluoroprop-1-ene [R-1234ze(E)], 4.3 mass fraction (%) 1,1,1,2,3,3,3-heptafluoropropane (R-227ea), and 17.0 mass fraction (%) R-1336mzz(E), is regarded as a potential alternative to 1,1,1,2-tetrafluoroethane (R-134a) [5].

Although property information on R-1336mzz(E) has been quite limited since it was first proposed, Sakoda et al. [6] recently made extensive measurements of thermodynamic properties of R-1336mzz(E), including the critical parameters, vapor pressures, saturated liquid and vapor densities, and (p, ρ, T)

behavior in both liquid and vapor phases. Based on these experimental data, this work developed the first fundamental equation of state expressed explicitly in the Helmholtz energy. This equation was successfully employed in subsequent studies for R-1336mzz(E) [7–9]. This paper presents the formulation of the equation of state and demonstrates comparisons to experimental data and behavior in the critical and extrapolated regions. In addition, an extended corresponding states (ECS) model employing the equation of state is given for the viscosity and thermal conductivity of R-1336mzz(E), and deviation plots between experimental and calculated values are presented.

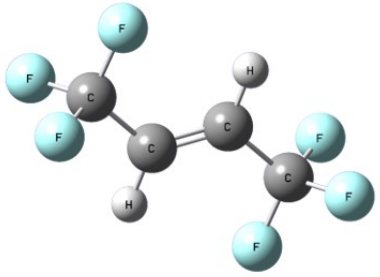

Fig. 1 Molecular structure of R-1336mzz(E) obtained from the geometry optimization with Gaussian 09 [10]

Table 1 Fundamental properties of R-1336mzz(E)

Property	Symbol	Value	Reference
CAS number		66711-86-2	
Chemical formula		*trans*-$CF_3CH{=}CHCF_3$	
Molar mass	M	164.0491 $g \cdot mol^{-1}$	
Critical temperature	T_c	403.53 K	Sakoda et al. [6]
Critical pressure	p_c	2.7790 MPa	This work
Critical density	ρ_c	3.129 $mol \cdot dm^{-3}$	This work
Triple-point temperature	T_{tp}	200.15 K	Tomassetti et al. [11]
Normal boiling-point temperature	T_{nbp}	281.02 K	This work
Acentric factor	ω	0.413	This work
Total atmospheric lifetime		0.334 yrs	Kayukawa et al. [12]
GWP (100-yr)		16	Kayukawa et al. [12]

2 Ancillary equations

Ancillary equations are presented for the vapor pressure and saturated liquid and vapor densities. These equations were formulated by fitting values calculated with the final equation of state. They provide rapid calculations of very close estimates of the saturation properties and give excellent initial guesses for the iterative process that finds rigorous solutions for the saturation state from the full equation of state based on the Maxwell criterion. Coefficients n_i of each equation are given in Table 2.

The vapor pressure p_s is correlated with the equation

$$\ln\left(\frac{p_\mathrm{s}}{p_\mathrm{c}}\right) = \frac{T_\mathrm{c}}{T}\left(n_1\theta + n_2\theta^{1.5} + n_3\theta^{1.88} + n_4\theta^{4.47}\right), \tag{1}$$

where T_c and p_c are the critical temperature (403.53 K) and pressure (2.7790 MPa), and $\theta = 1 - T/T_\mathrm{c}$. The saturated liquid and vapor densities (ρ' and ρ'') are represented as

$$\frac{\rho'}{\rho_\mathrm{c}} = 1 + n_1\theta^{0.347} + n_2\theta^{1.42} + n_3\theta^{1.82} + n_4\theta^{2.232} \tag{2}$$

and

$$\ln\left(\frac{\rho''}{\rho_\mathrm{c}}\right) = n_1\theta^{0.387} + n_2\theta^{1.34} + n_3\theta^{3.77} + n_4\theta^{7.85}, \tag{3}$$

where ρ_c is the critical density (3.129 $\mathrm{mol \cdot dm^{-3}}$). Figure 2 shows deviations in values calculated with Eqs. (1), (2), and (3) from the rigorous Maxwell solutions obtained with the full equation of state. The AADs (defined later) in p_s, ρ', and ρ'' from the triple-point temperature to the critical temperature are 0.0070 %, 0.024 %, and 0.013 %, respectively.

Table 2 Coefficients of Eqs. (1), (2), and (3).

	Eq. (1)	Eq. (2)	Eq. (3)
n_1	−8.2611	2.1958	−3.1511
n_2	3.9076	6.4706	−9.2173
n_3	−3.9675	−13.191	−32.976
n_4	−6.1565	7.7906	−86.791

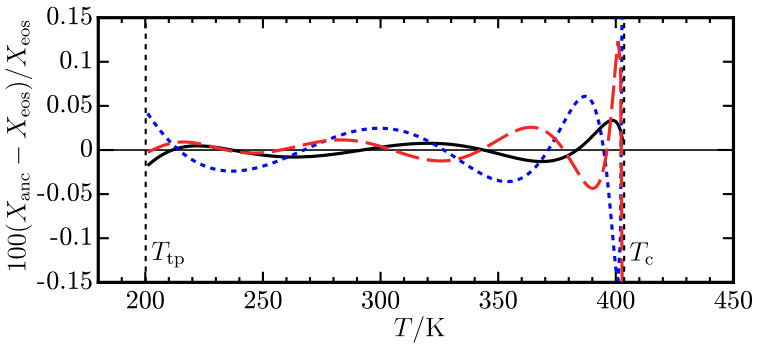

Fig. 2 Relative deviations in vapor pressures, saturated liquid densities, and saturated vapor densities calculated with the ancillary equations (X_{anc}) from the Maxwell solutions of the full equation of state (X_{eos}): (black solid line) vapor pressure; (blue dotted line) saturated liquid density; (red dashed line) saturated vapor density.

3 Equation of State

The equation of state for R-1336mzz(E) has the form

$$\frac{a(T,\rho)}{RT} = \alpha(\tau,\delta) = \alpha^{\circ}(\tau,\delta) + \alpha^{\mathrm{r}}(\tau,\delta), \tag{4}$$

where $R = 8.314462618\ \mathrm{J\cdot mol^{-1}\cdot K^{-1}}$ is the molar gas constant [13], a is the molar Helmholtz energy, α is the dimensionless Helmholtz energy, $\tau = T_{\mathrm{c}}/T$ is the reciprocal reduced temperature, and $\delta = \rho/\rho_{\mathrm{c}}$ is the reduced density. The critical temperature T_{c} is 403.53 K, which is the experimental value determined by Sakoda et al. [6]. The critical density ρ_{c} is 3.129 $\mathrm{mol\cdot dm^{-3}}$, and was obtained from the fitting of the equation of state starting from the experimental value (3.127 $\mathrm{mol\cdot dm^{-3}}$) [6]. The final equation of state calculates the

critical pressure as 2.7790 MPa at 403.53 K and 3.129 mol $\cdot$ dm^{-3}, which is in excellent agreement with the experimental value (2.7792 MPa) [6].

The dimensionless Helmholtz energy α is split into an ideal-gas part α° representing ideal-gas properties and a residual part α^{r} corresponding to the influence of intermolecular forces. They are often individually formulated. According to the ideal-gas law, the dimensionless ideal-gas Helmholtz energy α° is analytically derived from an equation for the ideal-gas isobaric heat capacity c_p° as follows:

$$\alpha^{\circ}(\tau,\delta) = \frac{h_0^{\circ}\tau}{RT_{\mathrm{c}}} - \frac{s_0^{\circ}}{R} - 1 + \ln\frac{\delta\tau_0}{\delta_0\tau} - \frac{\tau}{R}\int_{\tau_0}^{\tau}\frac{c_p^{\circ}}{\tau^2}\mathrm{d}\tau + \frac{1}{R}\int_{\tau_0}^{\tau}\frac{c_p^{\circ}}{\tau}\mathrm{d}\tau, \qquad (5)$$

where $\tau_0 = T_{\mathrm{c}}/T_0$, $\delta_0 = \rho_0/\rho_{\mathrm{c}} = p_0/(RT_0\rho_{\mathrm{c}})$, T_0 is the temperature at a reference state, p_0 is a reference pressure for the ideal-gas properties, and ρ_0 is the ideal-gas density at T_0 and p_0. The Planck-Einstein form is used in this work to represent the c_p° equation, which is given by

$$\frac{c_p^{\circ}}{R} = n_0^{\circ} + \sum_{i=1}^{2} n_i^{\circ}\left(\frac{m_i^{\circ}}{T}\right)^2 \frac{\exp(m_i^{\circ}/T)}{[\exp(m_i^{\circ}/T)-1]^2}\,. \qquad (6)$$

The coefficients m_i° and n_i° were initially determined from the experimental c_p° data of Kano et al. [14] and further adjusted while fitting vapor-phase sound speed data. The final values of n_i° and m_i° are given in Table 3. The final equation of state represents the experimental c_p° data [14] with an AAD (defined later) of 1.01 %.

The molecule of R-1336mzz(E) has 30 vibration modes; this number is almost equal to the sum of n_1° and n_2° (30.034). The ideal-gas Helmholtz energy

derived from Eqs. 5 and 6 is expressed in the form

$$\alpha^{\circ}(\tau,\delta) = \ln\delta + n_3^{\circ} + n_4^{\circ}\tau + (n_0^{\circ}-1)\ln\tau + \sum_{i=1}^{2} n_i^{\circ} \ln\left[1-\exp\left(-\frac{m_i^{\circ}\tau}{T_{\mathrm{c}}}\right)\right]. \quad (7)$$

The values of n_3° and n_4° are also given in Table 3, which were determined so that the specific enthalpy and entropy of the saturated liquid state at 0 °C are 200 $\mathrm{kJ \cdot kg^{-1}}$ and 1 $\mathrm{kJ \cdot kg^{-1} \cdot K^{-1}}$, respectively, corresponding to the common convention of the refrigeration industry; this is the standard reference state of the International Institute of Refrigeration (IIR). Table 3 gives additional digits for n_3° and n_4° in order to exactly reproduce these enthalpy and entropy values specified at the reference state.

Table 3 Coefficients and exponents of Eqs. 6 and 7 for R-1336mzz(E).

i	n_i°	m_i°
0	4.0	-
1	15.891	550.0
2	14.143	3474.0
3	−17.5838598852	-
4	11.5244170129	-

The dimensionless residual Helmholtz energy α^{r} is given by

$$\begin{aligned}\alpha^{\mathrm{r}}(\tau,\delta) = &\sum_{i=1}^{5} n_i \tau^{t_i} \delta^{d_i} + \sum_{i=6}^{10} n_i \tau^{t_i} \delta^{d_i} \exp(-\delta^{l_i}) \\ &+ \sum_{i=11}^{15} n_i \tau^{t_i} \delta^{d_i} \exp\left[-\eta_i(\delta-\varepsilon_i)^2 - \beta_i(\tau-\gamma_i)^2\right]. \end{aligned} \quad (8)$$

This form is empirical, and the number of terms and the coefficients and exponents are generally determined by fitting experimental data. This work used the nonlinear least-squares fitting technique originally developed by Lemmon and Jacobsen [15], where various thermodynamic constraints were also applied to ensure physically correct behavior over wide ranges of temperature

and pressure; this allows for the development of equations of state with reasonable extrapolation behavior, even if available experimental data are limited. The fitting techniques have been greatly extended by collaborations between correlators [16–21] over the last decade. Akasaka and Lemmon [22] and Lemmon and Akasaka [23] give an overview of the recent techniques, including an objective function minimized in the fitting and adequate thermodynamic constraints. Romeo and Lemmon [24] present a set of constraints used in the fitting for *n*-hexadecane, which includes constraints for the behavior of sound speed, isochoric heat capacity, rectilinear diameter, phase identification parameter [25], fourth virial coefficient, ideal curve, Joule inversion curve, and Joule-Thomson inversion curve. Some of these constraints were also applied to this work. The final values for the coefficients and exponents in Eq. 8 are given in Table 4. The large number of digits for n_3 and n_4 are given to accurately reproduce the following conditions at the critical point:

$$\left(\frac{\partial p}{\partial v}\right)_{T=T_c} = \left(\frac{\partial^2 p}{\partial v^2}\right)_{T=T_c} = 0. \tag{9}$$

4 Comparison to Experimental Data

Available experimental data for R-1336mzz(E) are summarized in Table 5. They are compared to calculated properties with the equation of state. The quality of the fit is evaluated mainly by comparing expanded experimental uncertainties at the 95 % confidence interval ($k = 2$) to average absolute deviations (AADs) in calculated properties. The AAD in any dataset X is

Table 4 Coefficients and exponents of Eq. 8 for R-1336mzz(E).

i	n_i	t_i	d_i	l_i	η_i	β_i	γ_i	ε_i
1	0.08297005	1.0	4					
2	1.1213658	0.117	1					
3	−2.0279038680756	1.0	1					
4	−0.3486706213113	1.0	2					
5	0.13227952	0.413	3					
6	−1.3751844	2.44	1	2				
7	−1.3939029	2.51	3	2				
8	0.11190839	0.535	2	1				
9	−0.90635088	1.927	2	2				
10	−0.050014594	1.186	7	1				
11	1.7953748	0.876	1		1.234	1.237	1.21	1.23
12	2.0579712	1.23	1		1.34	0.384	2.0	0.751
13	−1.0433081	0.875	3		1.13	1.24	1.216	0.522
14	−1.2459808	0.5181	2		1.15	0.46	2.27	0.32
15	−0.49712249	0.86	2		1.3	1.326	1.26	1.22

defined as

$$\mathrm{AAD}_X = \frac{100}{N_{\mathrm{exp}}} \sum_{i=1}^{N_{\mathrm{exp}}} \left| \frac{X_{i,\,\mathrm{exp}} - X_{i,\,\mathrm{calc}}}{X_{i,\,\mathrm{exp}}} \right|, \tag{10}$$

where N_{exp} is the number of data points in the dataset, $X_{i,\,\mathrm{exp}}$ is the i^{th} experimental value, and $X_{i,\,\mathrm{calc}}$ is the calculated value at the state conditions for $X_{i,\,\mathrm{exp}}$. For the vapor pressures, the absolute differences ($|X_{i,\,\mathrm{exp}} - X_{i,\,\mathrm{calc}}|$) are also considered.

4.1 Vapor Pressure

Figure 3 shows relative deviations and differences between experimental vapor pressures and values calculated with the equation of state. Four datasets are currently available. The data of Sakoda et al. [6] are located at temperatures from 287 K to the critical temperature; they are represented with an AAD of 0.05 %. All data points below 375 K are represented within the experimental uncertainty (1 kPa). At higher temperatures, larger differences up to 3.1 kPa

Table 5 Available experimental data for the thermophysical properties of R-1336mzz(E).

Author	Year	N	Range T/K	Range p/MPa	AAD/%
Vapor pressure					
Tanaka et al. [26]	2017	17	323–403		0.15
Kimura [27]	2019	14	300–390		2.22
Boonaert et al. [28]	2020	17	278–356		0.70
Sakoda et al. [6]	2021	26	287–403		0.05
Saturated liquid density					
Tanaka et al. [26]	2017	11	323–402		2.00
Sakoda et al. [6]	2021	11	329–403		0.72
Saturated vapor density					
Tanaka et al. [26]	2017	4	361–402		3.42
Sakoda et al. [6]	2021	10	342–403		0.68
(p, ρ, T) *data*					
Tanaka et al. [29]	2017	156	323–524	0.58–10.2	1.69[a]
Kimura [27]	2019	126	280–400	0.1–10.0	1.32[a]
Sakoda et al. [6]	2021	40	300–410	0.21–5.7	0.20[a]
Isobaric heat capacity					
Kagawa and Matsuguchi [30]	2022	33	308–363	0.20–1.00	6.72
Sound speed					
Kano et al. [14]	2019	36	303–393	0.04–0.90	0.02
Peng et al. [31]	2022	98	298–363	0.12–0.81	0.22
Kano [32]	2022	36	303–403	0.04–0.90	0.04
Ideal-gas isobaric heat capacity					
Kano et al. [14]	2019	6	303–393		1.01
Peng et al. [31]	2022	13	303–363		7.52
Kano [32]	2022	6	303–403		2.71
Viscosity					
Mondal et al. [9]	2022	92	314–452	1.00–4.03	2.01[b]
Thermal conductivity					
Mondal et al. [8]	2021	208	313–453	0.24–4.07	1.29[b]

[a] Deviation in density
[b] Deviation from the ECS model

are observed, but their relative deviations are still less than 0.12 %; this is sufficiently accurate. The data of Tanaka et al. [26] are almost consistent with those of Sakoda et al. [6]; the AAD in the data is 0.15 %, and all data points are expressed within their experimental uncertainty (4.5 kPa). The data of Boonaert et al. [28] show systematic positive deviations; the AAD in the data is 0.70 %, and the largest deviation is 1.64 % at 283 K. Differences over the experimental uncertainty (1 kPa) are often observed. The data of Kimura [27]

are quite inconsistent with the other datasets, probably due to lower purity (98.8 mol %), and they are off-scale in most cases.

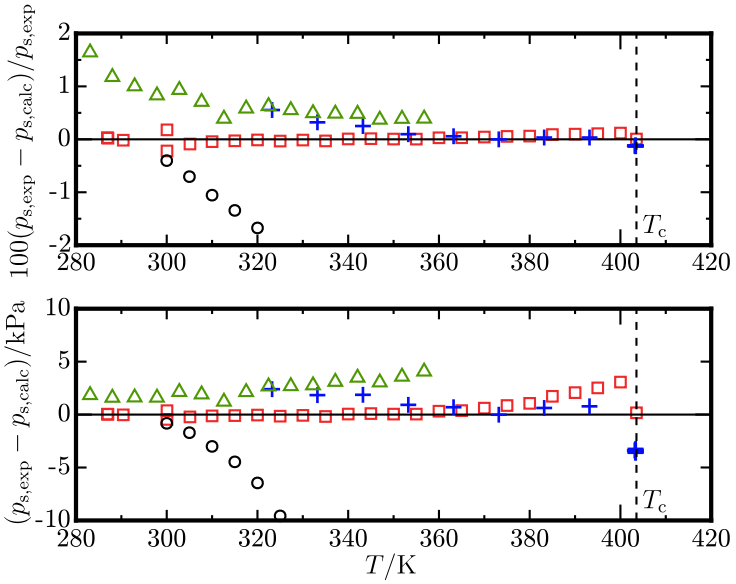

Fig. 3 Relative deviations (top panel) and absolute differences (bottom panel) between experimental vapor pressures and values calculated with the equation of state: (+) Tanaka et al. [26]; (○) Kimura [27]; (△) Boonaert et al. [28]; (□) Sakoda et al. [6]

4.2 Saturated liquid and vapor densities

Figure 4 shows the saturation boundary calculated from the equation of state on a T-ρ diagram, along with experimental data of the saturated liquid and vapor densities [6,29]. The calculated boundary reasonably represents the experimental data of Sakoda et al. [6]; the AADs in the data are 0.72 % for the saturated liquid densities and 0.69 % for the saturated vapor densities, which exceed the experimental uncertainties (0.06 % to 0.24 %) but are acceptable in most engineering applications. The saturated vapor densities of Tanaka et

al. [29] are consistent with those of Sakoda et al. [6], but inconsistency is observed in the saturated liquid densities of these two datasets. As a result, the saturated liquid densities of Tanaka et al. [29] often show deviations over 2 % from values calculated with the equation. Although Tanaka et al. [29] do not clearly state the experimental uncertainties in their measurements, the saturated liquid densities probably include high uncertainties because they came from the extrapolation of liquid isochores determined from only two or three data points.

The rectilinear diameter (indicated by the dashed line), the mean value of saturated liquid and vapor densities, is almost straight up to the critical temperature; this is thermodynamically reasonable behavior.

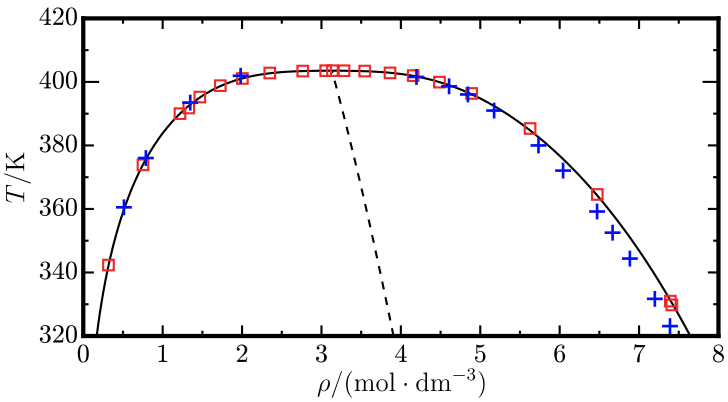

Fig. 4 Saturation boundary calculated from the equation of state and experimental data of the saturated liquid and vapor densities: (+) Tanaka et al. [29]; (□) Sakoda et al. [6]. The dashed line indicates the rectilinear diameter.

4.3 (p, ρ, T) behavior

Three experimental datasets are available for the (p, ρ, T) behavior. Figure 5 shows their density deviations from values calculated with the equation of state. Experimental uncertainties in the data of Sakoda et al. [6] are the smallest among these datasets, which are 0.005 K, 1.0 kPa, and 0.15 % in the temperature, pressure, and density measurements. The equation of state represents these data well; the AADs in density are 0.32 % for the vapor phase and 0.13 % for the liquid phase, and the overall AAD is 0.20 %, which is comparable to the experimental uncertainty. In addition, good consistency is observed between the (p, ρ, T) data of Sakoda et al. [6] and their vapor pressure data. The data of Tanaka et al. [29], on the other hand, are more scattered due to larger experimental uncertainties, which are 0.03 K, 4 kPa, and 0.4 % in the temperature, pressure, and density measurements. The liquid densities show substantial systematic negative deviations that sometimes exceed −3 %. The AADs are 0.72 %, 2.65 %, and 1.56 % for the vapor, liquid, and supercritical regions, respectively, and the overall AAD is 1.69 %. The vapor-phase (p, ρ, T) data of Kimura [27] follow a similar trend to those of Sakoda et al. [6], but the liquid phase data show systematic negative deviations down to −2 %. The AADs for the vapor and liquid phases are 1.84 % and 0.62 %, respectively, and the overall AAD is 1.32 %. Kimura [27] claims that the expanded uncertainty in the density measurement is 0.076 % at the highest pressure (10 MPa); however, higher uncertainties, which come from lower sample purity or experimental errors, could be included in their measurements.

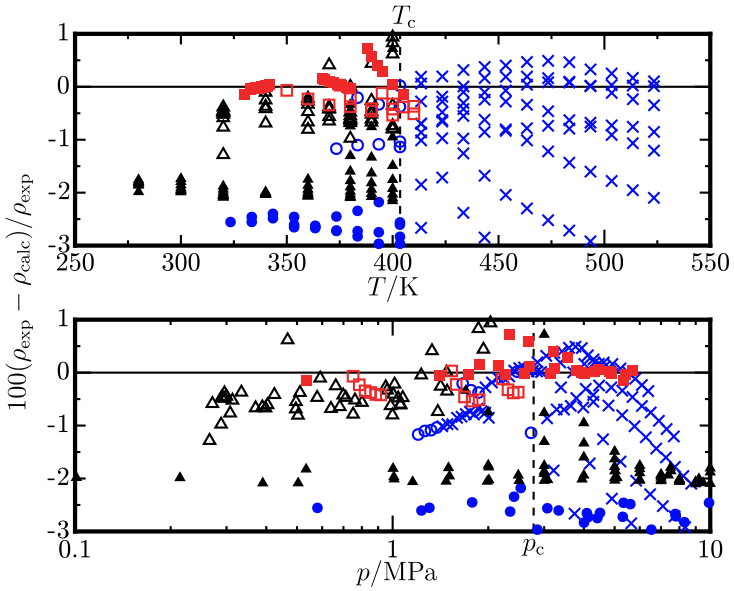

Fig. 5 Relative density deviations in the experimental (p, ρ, T) data from values calculated with the equation of state: (○) Tanaka et al. [29] (vapor); (●) Tanaka et al. [29] (liquid); (×) Tanaka et al. [29] (supercritical); (△) Kimura [27] (vapor); (▲) Kimura [27] (liquid); (□) Sakoda et al. [6] (vapor); (■) Sakoda et al. [6] (liquid).

4.4 Caloric Data

Three datasets are currently available for vapor-phase sound speeds. Figure 6 shows their deviations from values calculated with the equation of state. Kano et al. [14] measured with an acoustic-microwave resonator with a cylindrical cavity, and the experimental uncertainties were roughly estimated as 0.1 % at most. The equation accurately represents the data with an AAD of 0.02 %, and no systematic deviations are observed. Recently, Kano [32] slightly revised the first data [14] taking the effect of impurity into account. The final experimental uncertainties were determined as a maximum of 0.048 %, which is similar to the AAD from calculated values. Peng et al. [31] also measured vapor-phase sound speeds with a cylindrical acoustic resonator; however, inconsistency is

observed between their data and those of Kano et al. [14] and Kano [32]. The data of Peng et al. [31] show systematic negative deviations down to −0.3 %, although their experimental uncertainty is claimed as 0.015 %.

Kagawa and Matsuguchi [30] measured isobaric heat capacities in the vapor phase with a flow calorimeter. They estimated the experimental uncertainties as 1.9 % to 3.7 %, but most data points show larger deviations from values calculated with the equation of state; the AAD is 6.72 %.

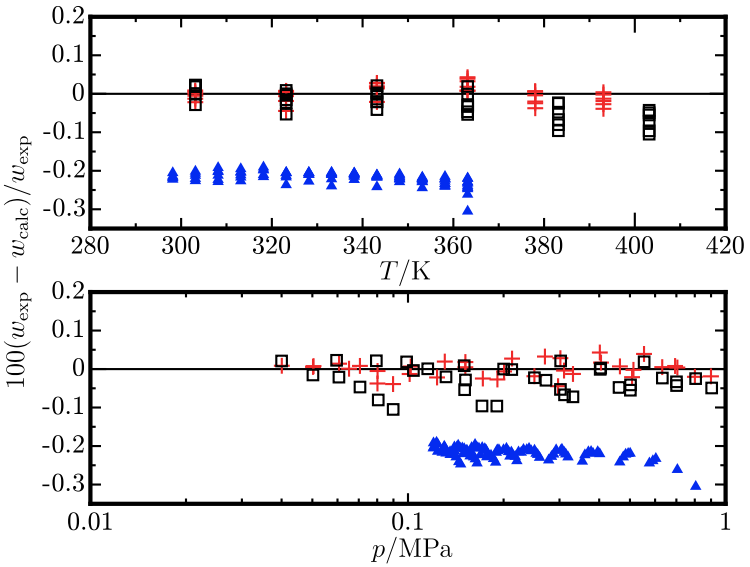

Fig. 6 Relative deviations in experimental vapor-phase sound speed data from values calculated with the equation of state: (+) Kano et al. [14]; (▲) Peng et al. [31]; (□) Kano [32].

5 Behavior in the Critical and Extrapolated Regions

Derived properties calculated from higher-order derivatives of the Helmholtz energy are generally sensitive to underlying problems in equations of state, and

therefore their plots on various thermodynamic coordinates are often used to verify the behavior of the equations in the critical and extrapolated regions; this is particularly essential for equations formulated from limited experimental data, such as the equation developed in this work. Several examples are given here.

5.1 Virial coefficients

Virial coefficients are the most fundamental properties representing the attractive and repulsive forces between molecules in the vapor phase. Equations of state should adequately represent the trends of virial coefficients, even if their experimental values are unavailable. The fitting process in this work consistently monitored and controlled the values, slopes, and curvatures of the second, third, and fourth virial coefficients. They are related to density derivatives of the residual Helmholtz energy as the density approaches zero; for example, the fourth virial coefficient D is given by

$$D = \lim_{\rho \to 0} \left[\frac{1}{2RT} \left(\frac{\partial^3 a^{\mathrm{r}}}{\partial \rho^3} \right)_T \right] = \lim_{\delta \to 0} \left[\frac{1}{2\rho_{\mathrm{c}}^3} \left(\frac{\partial^3 \alpha^{\mathrm{r}}}{\partial \delta^3} \right)_\tau \right], \tag{11}$$

where a^{r} is the residual Helmholtz energy. Figure 7 shows trends in the virial coefficients obtained from the equation of state over a wide range of temperature. These changes qualitatively agree with those theoretically expected by Thol et al. [33] from the analysis of the Lennard-Jones fluid; specifically, B and C go to negative infinity at zero temperature, pass through zero at a moderate temperature, increase to a maximum, and approach zero at extremely

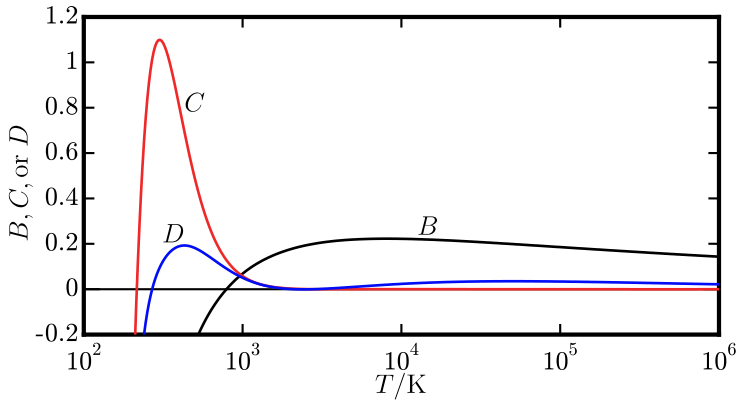

Fig. 7 Second, third, and fourth virial coefficients (B, C, and D) derived from the equation of state. The values along the y-axis are equal to those of B, $10C$, and $100D$, and their units are $\mathrm{dm^3 \cdot mol^{-1}}$, $\mathrm{dm^6 \cdot mol^{-2}}$, and $\mathrm{dm^9 \cdot mol^{-3}}$, respectively.

high temperatures. The theoretical trend in D is similar to those in B and C, but there is a second maximum with a smaller magnitude.

5.2 Heat capacities

The isochoric and isobaric heat capacities drastically change in the critical region and diverge to infinity at the critical point. Experimental heat capacity data in the critical region are normally unavailable for most industrial fluids; nevertheless, equations of state should qualitatively represent not only these drastic changes in the critical region but give physically correct behavior over wide ranges of temperature and pressure. During the fitting in this work, high priority was given to controlling the slopes and curvatures of the heat capacities. Figure 8 shows the residual isochoric heat capacities c_v^{r} $(= c_v - c_v^{\circ})$ versus temperature along the saturation lines, isobars, and the critical isochore. This figure demonstrates reasonable behavior of the equation of state both in the

critical and extrapolated regions. The critical isochore monotonically decreases from the critical point to higher temperatures, which means that temperature derivatives of the residual Helmholtz energy are properly formulated because the isochoric heat capacity is calculated only from the second partial derivative of the Helmholtz energy with respect to temperature.

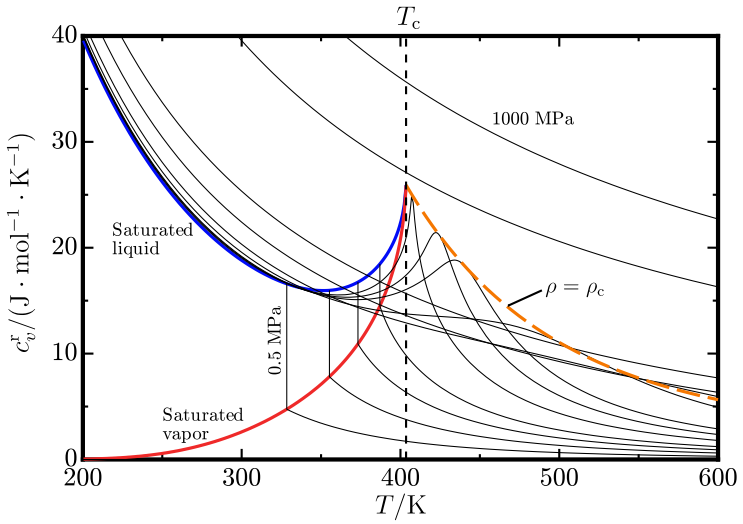

Fig. 8 Residual isochoric heat capacity (c_v^r) versus temperature along isobars at 0.5, 1, 1.5, 2, 3, 4, 5, 10, 20, 50, 100, 500, 1000 MPa, saturation boundaries (blue and red lines), and the critical isochore ($\rho = \rho_c$) (dashed orange line).

5.3 Ideal curves

Four characteristic curves (ideal curve, Boyle curve, Joule-Thomson inversion curve, and Joule inversion curve) are obtained from derivatives of the compressibility factor $Z = p/(\rho RT)$, as given in Table 6. Plots of these curves on a p-T diagram are often used to confirm the (p, ρ, T) behavior over wide ranges of temperature and pressure. The fitting process in this work occasion-

ally verified the shapes of these curves, and if a physically incorrect bump was found along a curve, then the fitting process attempted to fix it by directly controlling its various derivatives. Figure 9 shows the four characteristic curves obtained from the equation of state. All curves exhibit smooth shapes in general, and no unnatural bumps are observed; this indicates that the equation of state would provide reasonable extrapolation of the (p, ρ, T) behavior.

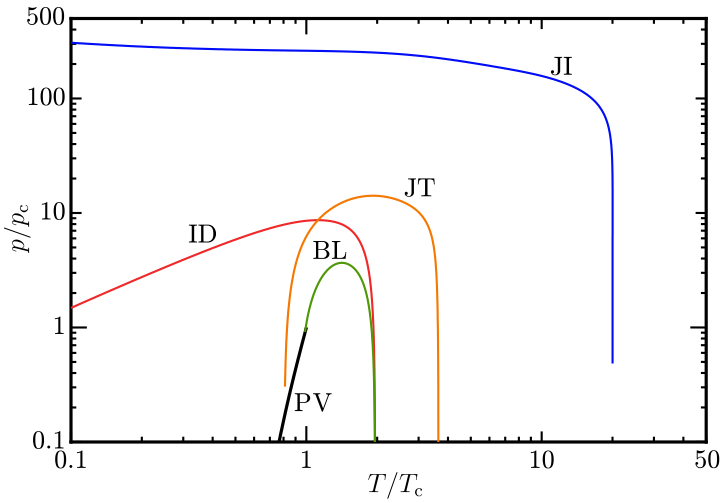

Fig. 9 Four characteristic curves and the vapor pressure curve (PV). ID: ideal curve; BL: Boyle curve; JT: Joule-Thomson inversion curve; JI: Joule inversion curve.

Table 6 Four characteristic curves.

Designation	Definition
Ideal curve	$Z = 1$
Boyle curve	$\left(\frac{\partial Z}{\partial \rho}\right)_T = 0$
Joule-Thomson inversion curve	$\left(\frac{\partial Z}{\partial T}\right)_p = 0$
Joule inversion curve	$\left(\frac{\partial Z}{\partial T}\right)_\rho = 0$

5.4 Phase identification parameter

The phase identification parameter (PIP) [25], which was originally used to distinguish whether a state point is in the vapor or liquid phase, is one of the most sensitive properties to identify incorrect behavior in an equation of state because it is calculated from several higher-order derivatives of the Helmholtz energy. The PIP is defined as

$$\mathrm{PIP} = 2 - \rho \left[\frac{\dfrac{\partial^2 p}{\partial \rho \partial T}}{\left(\dfrac{\partial p}{\partial T}\right)_\rho} - \frac{\left(\dfrac{\partial^2 p}{\partial \rho^2}\right)_T}{\left(\dfrac{\partial p}{\partial \rho}\right)_T} \right] . \tag{12}$$

The fitting process often inspected the PIP along various isotherms from very low to extremely high temperatures. Unnatural bumps and inflection points were removed by adjusting derivatives of the isotherms. Figure 10 shows the PIP calculated from the equation of state versus temperature along isobars from 0.5 MPa to 1000 MPa. The saturation lines and isobars are smooth over wide ranges of temperature and pressure, and no unreasonable behavior is observed.

6 Extended Corresponding States Model for Transport Properties

For a complete description of thermophysical properties for engineering calculations, one also needs models for the surface tension, viscosity, and thermal conductivity. Iwasaki et al. [34] developed a model for surface tension for R-1336mzz(E). Yang et al. [35] applied a viscosity model based on the residual entropy scaling theory to various fluids including refrigerants. Here we present

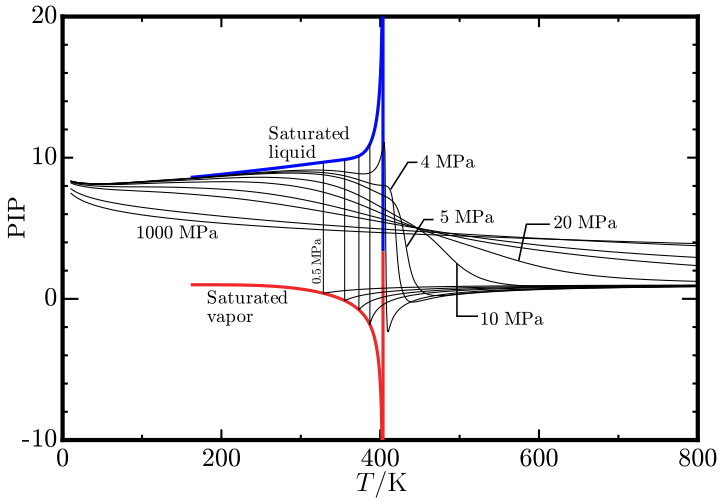

Fig. 10 Phase identification parameter (PIP) versus temperature along isobars at 0.5, 1, 1.5, 2, 3, 4, 5, 10, 20, 50, 100, 500, 1000 MPa, and the saturated liquid and saturated vapor lines (blue and red curves).

extended corresponding states (ECS) models for the viscosity and thermal conductivity based on the Helmholtz energy equation of state developed in this work. Following the methodology by Huber [36], adjustable parameters of the ECS model were fitted to the experimental thermal conductivity and viscosity data of Mondal et al. [8,9]. Details of the ECS model are given elsewhere [36], and only the fitted parameters are summarized here.

6.1 Viscosity

The Lennard-Jones collision diameter σ and the Lennard-Jones pair-potential energy ε, which are used to estimate the dilute-gas viscosity, were determined using the estimation method of Chung et al. [37]. They are $\sigma = 0.5531$ nm and $\varepsilon/k_{\mathrm{B}} = 320.44$ K, where k_{B} is the Boltzmann constant. A conformal molar density of the reference fluid (R-134a) determined according to the ECS model

is modified with the correction factor ψ given by

$$\psi(\delta) = c_0 + c_1\delta, \tag{13}$$

where δ is the reduced density ($\delta = \rho/\rho_c$) of the fluid of interest [R-1336mzz(E)], $c_0 = 1.0576$, and $c_1 = -1.62884 \times 10^{-2}$. In addition, a vapor phase correction F_c for molecular structure and polar effects introduced by Chung et al. [37] was determined to be 0.761917. The parameters c_0, c_1, and F_c were found by fitting the complete data set of Mondal et al. [9] that included points in the liquid, vapor, and supercritical states. Figure 11 shows deviations in the experimental viscosities [9] from values calculated with the ECS model. While the expanded uncertainties claimed by the author are 2.30 % for the vapor phase, 2.26 % for the liquid phase, and 2.32 % for the supercritical region, the AADs from the ECS model are 2.26 %, 1.04 %, and 3.37 %, respectively. The overall AAD (2.01 %) is comparable to the expanded uncertainties, and no systematic deviation is observed.

6.2 Thermal conductivity

The adjustable parameter f_{int} of the Eucken correlation for the internal contribution (due to internal motions of molecules) to thermal conductivity was fitted to thermal conductivity data [8], and given as a polynomial function of temperature

$$f_{int} = n_0 + n_1 T + n_2 T^2, \tag{14}$$

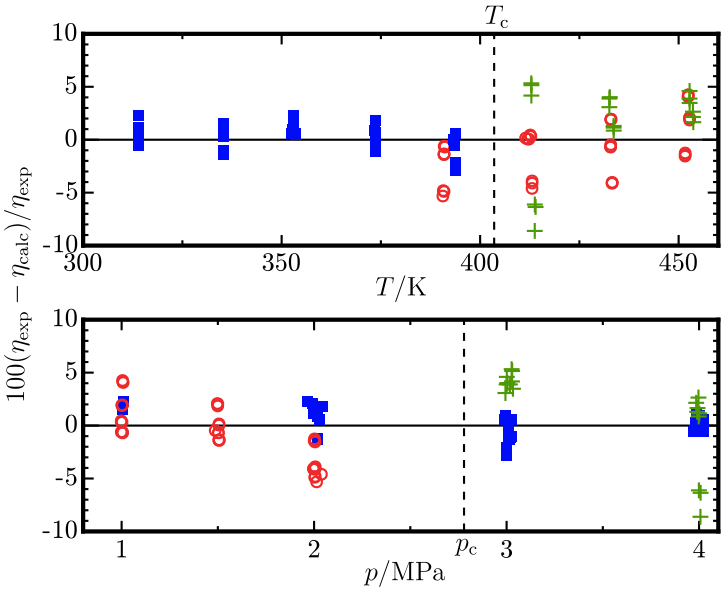

Fig. 11 Relative deviations in the experimental viscosities [9] from values calculated with the ECS model: (○) vapor; (■) liquid; (+) supercritical.

where $n_0 = 6.14979 \times 10^{-3}$, $n_1 = -2.33715 \times 10^{-5}$, and $n_2 = 2.89125 \times 10^{-8}$. The correction factor χ for a conformal molar density of the reference fluid (R-134a) is given by

$$\chi(\delta) = b_0 + b_1\delta, \tag{15}$$

where $b_0 = 1.65952$ and $b_1 = -0.230647$. Values for the parameters n_0, n_1, n_2, b_0, and b_1 were determined by fitting the entire experimental data set [8]. Figure 12 shows deviations between the experimental thermal conductivities [8] and values calculated with the ECS model. The expanded uncertainties claimed by the author are 1.98 % for the vapor phase, 1.94 % for the liquid phase, and 2.01 % for the supercritical region, and the ECS model calculates those with AADs of 1.26 %, 0.89 %, and 2.61 %, respectively. Only three data points for the vapor phase near 394 K and 2.0 MPa show particularly

large deviations over 7 %; however, the overall AAD (1.29 %) is less than the expanded uncertainties, and no systematic deviation is observed.

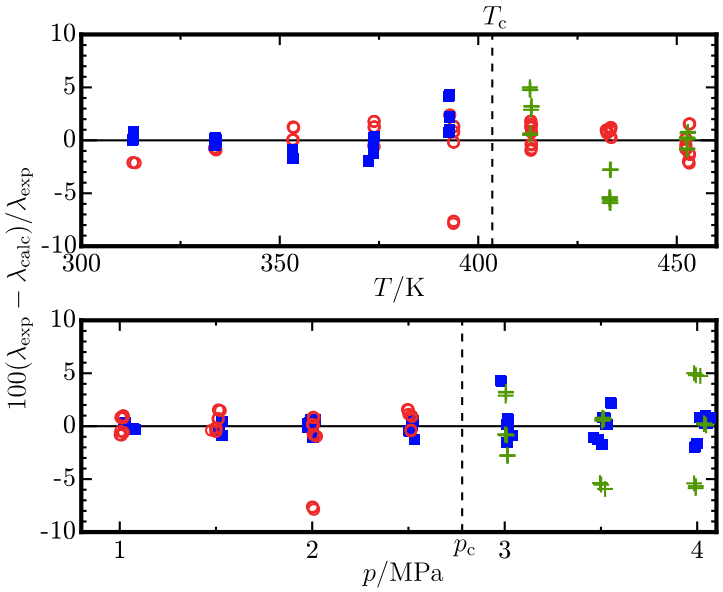

Fig. 12 Relative deviations in the experimental thermal conductivities [8] from values calculated with the ECS model: (○) vapor; (■) liquid; (+) supercritical.

7 Conclusions

The first Helmholtz energy equation of state for R-1336mzz(E) was developed from the consistent experimental datasets for the critical parameters, vapor pressure, saturated liquid and vapor densities, (p, ρ, T) behavior, vapor-phase sound speed, and ideal-gas isobaric heat capacity. The equation of state is valid at temperatures from 200.15 K to 410 K and pressures up to 5.7 MPa. Comparisons to the experimental data concluded that expected relative uncertainties ($k = 2$) in this range are 0.1 % for vapor pressures, 1 % for saturated liquid

densities, 1 % for saturated vapor densities, 0.15 % for liquid densities, 0.5 % for vapor densities, and 0.05 % for vapor-phase sound speeds, except in the critical region where larger uncertainties of up to 2 % are sometimes observed in densities. Plots of various derived properties show that the equation exhibits reasonable behavior in the critical and extrapolated regions. The extended corresponding states (ECS) model for the viscosity and thermal conductivity of R-1336mzz(E) were also formulated by employing the equation of state. The model represents recent experimental data for these properties almost within their experimental uncertainties.

Although the equation of state and ECS model presented here are interim models based on limited experimental data, their expected uncertainties and extrapolation behavior suggest that they could be successfully used in most engineering applications such as the analyses of heat transfer and refrigeration cycle performance. We plan to update the equation and ECS model when additional measurements become available. Liquid densities and liquid-phase sound speeds at higher pressures are most needed.

As an aid in computer implementation, calculated property values from the equation of state are given in Table 7. Table 8 gives several points for checking the computer implementation of the viscosity and thermal conductivity models. Supporting Information provides a fluid file (R1336MZZE.FLD) for use in REFPROP [38] and TREND [39], a fluid file (R1336MZZE.json) for use in CoolProp [40], and Python code (R1336MZZE.py) to display the values

in Table 7. The REFPROP file can also be used to reproduce the values in Table 8 for viscosity and thermal conductivity.

Table 7 Calculated property values from the equation of state for R-1336mzz(E) to verify computer code.†

T (K)	ρ ($\mathrm{mol \cdot dm^{-3}}$)	p (MPa)	c_v ($\mathrm{J \cdot mol^{-1} \cdot K^{-1}}$)	c_p ($\mathrm{J \cdot mol^{-1} \cdot K^{-1}}$)	w ($\mathrm{m \cdot s^{-1}}$)
300	0	0	125.686	134.001	127.321
300	8.5	22.73753	146.214	193.851	725.684
300	0.05	0.119033	127.121	137.553	122.301
380	6	2.279713	154.022	254.161	209.403
380	0.5	1.212781	144.095	172.608	113.306
405	3	2.859345	165.611	4690.00	71.6230

†All values were calculated with REFPROP DLL 10.0.0.98.

Table 8 Calculated property values for viscosity and thermal conductivity for R-1336mzz(E) to verify computer code.†

T (K)	ρ ($\mathrm{mol \cdot dm^{-3}}$)	p (MPa)	η ($\mu\mathrm{Pa \cdot s}$)	λ ($\mathrm{mW \cdot m \cdot K^{-1}}$)
300	0	0	8.94906	12.4500
300	8.5	22.73753	401.367	75.8548
300	0.05	0.119033	8.85946	12.5160
380	6	2.279713	99.8964	53.4109
380	0.5	1.212781	11.8980	15.7678
405	3	2.859345	30.8929	53.7455

†All values were calculated with REFPROP DLL 10.0.0.98.

Acknowledgements The authors appreciate Mark O. McLinden, Allan H. Harvey, and Ian H. Bell, and Kehui Gao, National Institute of Standards and Technology, Boulder, for their assistance during the documentation of this paper. The authors are grateful to Ian H. Bell for his generous support in programming the supplementary computer codes.

Declarations

Competing interests

The authors declare that they have no conflict of interest.

Authors' contributions

RA contributed to evaluating available experimental data, fitting the consistent data to the final equation, and writing, reviewing, and editing the whole manuscript. MLH contributed to formulating the ECS model for the transport properties based on the final equation of state. LDS contributed to fitting an initial functional form of the equation of state. EWL contributed to establishing the fitting techniques for reliable equations of state and coding a computer program to implement it.

Funding

Partially funded by the National Institute of Standards and Technology

Availability of data and materials

not applicable

References

1. ANSI/ASHRAE Standard 34-2019; Designation and Safety Classification of Refrigerants (2019)
2. K. Kontmaris, , L.D. Simoni, in *Proceedings of JRAIA International Symposium* (Kobe, Japan, 2016), pp. 283–288
3. J.R. Juhasz, in *Proceedings of the 12^{th} IEA Heat Pump Conference* (Rotterdam, the Netherlands, 2017)
4. D.L. Murphy, M.S. Katancik, in *Proceedings of 25^{th} International Compressor Engineering Conference at Purdue (PaperID 2681)* (West Lafayette, IN, USA, 2021)
5. K. Gao, N. Purohit, E.V. Becerra, R. Vogl, A. Sethi, R. Hulse, in *Proceedings of 19^{th} International Refrigeration and Air Conditioning Conference at Purdue, (PaperID 2578)* (West Lafayette, IN, USA, 2022)

6. N. Sakoda, Y. Higashi, R. Akasaka, J. Chem. Eng. Data **66**(1), 734 (2021). DOI 10.1021/acs.jced.0c00848

7. M.A. Kedzierski, L. Lin, Pool Boiling of R514A, R1224yd(Z), and R1336mzz(E) on a Reentrant Cavity Surface; Extensive Measurement and Analysis. Tech. Rep. NIST Technical Note 2125, National Institute of Standards and Technology, Gaithersburg, MD, USA (2020). DOI 10.6028/NIST.TN.2125

8. D. Mondal, K. Kariya, A.R. Tuhin, K. Miyoshi, A. Miyara, Int. J. Refrig. **129**, 109 (2021). DOI 10.1016/j.ijrefrig.2021.05.005

9. D. Mondal, K. Kariya, A.R. Tuhin, N. Amakusa, A. Miyara, Int. J. Refrig. **133**, 267 (2022). DOI 10.1016/j.ijrefrig.2021.10.006

10. M.J. Frisch, G.W. Trucks, H.B. Schlegel, G.E. Scuseria, M.A. Robb, J.R. Cheeseman, G. Scalmani, V. Barone, B. Mennucci, G.A. Petersson, H. Nakatsuji, M. Caricato, X. Li, H.P. Hratchian, A.F. Izmaylov, J. Bloino, G. Zheng, J.L. Sonnenberg, M. Hada, M. Ehara, K. Toyota, R. Fukuda, J. Hasegawa, M. Ishida, T. Nakajima, Y. Honda, O. Kitao, H. Nakai, T. Vreven, J.A. Montgomery, Jr., J.E. Peralta, F. Ogliaro, M. Bearpark, J.J. Heyd, E. Brothers, K.N. Kudin, V.N. Staroverov, R. Kobayashi, J. Normand, K. Raghavachari, A. Rendell, J.C. Burant, S.S. Iyengar, J. Tomasi, M. Cossi, N. Rega, J.M. Millam, M. Klene, J.E. Knox, J.B. Cross, V. Bakken, C. Adamo, J. Jaramillo, R. Gomperts, R.E. Stratmann, O. Yazyev, A.J. Austin, R. Cammi, C. Pomelli, J.W. Ochterski, R.L. Martin, K. Morokuma, V.G. Zakrzewski, G.A. Voth, P. Salvador, J.J. Dannenberg, S. Dapprich, A.D. Daniels, O. Farkas, J.B. Foresman, J.V. Ortiz, J. Cioslowski, D.J. Fox. Gaussian 09 Revision D.01 (2009). Gaussian Inc. Wallingford CT 2009

11. S. Tomassetti, G. Di Nicola, C. Kondou, Int. J. Refrig. **133**, 172 (2022). DOI 10.1016/j.ijrefrig.2021.10.008

12. Y. Kayukawa, C. Kondou, N. Sakoda, K. Kariya, S. Fukuda, *JSRAE Thermodynamic Tables JARef Vol. 5: HFOs & HCFOs* (Japan Society of Refrigerating and Air Conditioning Engineers, 2021)

13. E. Tiesinga, P.J. Mohr, D.B. Newell, B.N. Taylor, J. Phys. Chem. Ref. Data **50**(3), 033105 (2021). DOI 10.1063/5.0064853
14. Y. Kano, Y. Kayukawa, Y. Fujita, in *Proceedings of the 2nd Pacific Rim Thermal Engineering Conference* (Hawaii, USA, 2019)
15. E.W. Lemmon, R.T. Jacobsen, J. Phys. Chem. Ref. Data **34**(1), 69 (2005). DOI 10.1063/1.1797813
16. K. Gao, J. Wu, P. Zhang, E.W. Lemmon, J. Chem. Eng. Data **61**(8), 2859 (2016). DOI 10.1021/acs.jced.6b00195
17. E.W. Lemmon, M.O. McLinden, W. Wagner, J. Chem. Eng. Data **54**(12), 3141 (2009). DOI 10.1021/je900217v
18. R. Akasaka, Y. Zhou, E.W. Lemmon, J. Phys. Chem. Ref. Data **44**(1), 013104 (2015). DOI 10.1063/1.4913493
19. M. Thol, E.W. Lemmon, Int. J. Thermophys. **37**(3), 28 (2016). DOI 10.1007/s10765-016-2040-6
20. S. Herrig, M. Thol, A.H. Harvey, E.W. Lemmon, J. Phys. Chem. Ref. Data **47**(4), 043102 (2018). DOI 10.1063/1.5053993
21. R. Akasaka, E.W. Lemmon, J. Chem. Eng. Data **64**(11), 4679 (2019). DOI 10.1021/acs.jced.9b00007
22. R. Akasaka, E.W. Lemmon, J. Phys. Chem. Ref. Data **51**(2), 023101 (2022). DOI 10.1063/5.0083026
23. E.W. Lemmon, R. Akasaka, Int. J. Thermophys. **43**(8), 119 (2022). DOI 10.1007/s10765-022-03015-y
24. R. Romeo, E.W. Lemmon, Int. J. Thermophys. **43**(10), 146 (2022). DOI 10.1007/s10765-022-03059-0
25. G. Venkatarathnam, L.R. Oellrich, Fluid Phase Equilib. **301**(2), 225 (2011). DOI 10.1016/j.fluid.2010.12.001
26. K. Tanaka, J. Ishikawa, K.K. Kontomaris, Int. J. Refrig. **82**, 283 (2017). DOI 10.1016/j.ijrefrig.2017.06.012
27. T. Kimura, Thermodynamic Properties of HFO Refrigerants as Working Fluid for High Temperature Heat Pump. Ph.D. thesis, Waseda University, Japan (2019)

28. E. Boonaert, A. Valtz, J. Brocus, C. Coquelet, Y. Beucher, F. De Carlan, J.M. Fourmigué, Int. J. Refrig. **114**, 210 (2020). DOI 10.1016/j.ijrefrig.2020.02.016
29. K. Tanaka, J. Ishikawa, K.K. Kontomaris, J. Chem. Eng. Data **62**(8), 2450 (2017). DOI 10.1021/acs.jced.7b00381
30. N. Kagawa, A. Matsuguchi, J. Chem. Eng. Data **67**(10), 2948 (2022). DOI 10.1021/acs.jced.2c00331
31. X. Peng, H. Liu, L. Xu, Z. Yang, Y. Duan, J. Chem. Thermodyn. **171**, 106808 (2022). DOI 10.1016/j.jct.2022.106808
32. Y. Kano, submitted to J. Chem. Eng. Data (2022)
33. M. Thol, G. Rutkai, A. Köster, R. Lustig, R. Span, J. Vrabec, J. Phys. Chem. Ref. Data **45**(2), 023101 (2016). DOI 10.1063/1.4945000
34. S. Iwasaki, C. Kondou, Y. Higashi, Trans. JSRAE **37**(1), 73 (2020). DOI 10.11322/tjsrae.19-36TG_EM_OA
35. X. Yang, X. Xiao, M. Thol, M. Richter, I.H. Bell, Int. J. Thermophys. **43**(12), 183 (2022). DOI 10.1007/s10765-022-03096-9
36. M.L. Huber, Models for Viscosity, Thermal Conductivity, and Surface Tension of Selected Pure Fluids as Implemented in REFPROP v10.0. Tech. Rep. NIST Interagency/Internal Report (NISTIR) 8209, National Institute of Standards and Technology, Gaithersburg, MD, USA (2018). DOI 10.6028/NIST.IR.8209
37. T.H. Chung, M. Ajlan, L.L. Lee, K.E. Starling, Ind. Eng. Chem. Res. **27**(4), 671 (1988). DOI 10.1021/ie00076a024
38. E.W. Lemmon, I.H. Bell, M.L. Huber, M.O. McLinden. NIST Standard Reference Database 23: Reference Fluid Thermodynamic and Transport Properties-REFPROP, Version 10.0, National Institute of Standards and Technology (2018). DOI 10.18434/T4/1502528. URL `https://www.nist.gov/srd/refprop`
39. R. Span, R. Beckmüller, S. Hielscher, A. Jäger, E. Mickoleit, T. Neumann, S. Pohl, B. Semrau, M. Thol. TREND. Thermodynamic Reference and Engineering Data 5.0. Lehrstuhl für Thermodynamik, Ruhr-Universität Bochum. (2020)
40. I.H. Bell, J. Wronski, S. Quoilin, V. Lemort, Ind. Eng. Chem. Res. **53**(6), 2498 (2014). DOI 10.1021/ie4033999